ACS APPLIED MATERIALS & INTERFACES

www.acsami.org

Research Article

Tuning Exchange Coupling in NiO-Based Bimagnetic Heterostructured Nanocrystals

Abdullah Al Shafe, Mohammad Delower Hossain, Robert A. Mayanovic,* Vladimir Roddatis, and Mourad Benamara

Cite This: *ACS Appl. Mater. Interfaces* 2021, 13, 24013–24023

Read Online

ACCESS | Metrics & More | Article Recommendations | Supporting Information

ABSTRACT: A series of bimagnetic heterostructured nanocrystals having an antiferromagnetic NiO core and a ferrimagnetic $Mn_xNi_{1-x}O$ and/or FiM Mn_3O_4 island nanophase overgrowth has been synthesized under varying aqueous solution pH conditions. The two-step self-assembly process employs a thermal decomposition method to synthesize NiO nanoparticles, followed by growth of the $Mn_xNi_{1-x}O$ and/or Mn_3O_4 nanophase over the NiO core using hydrothermal synthesis at pH values ranging from 2.4–7.0. The environmentally benign hydrothermal process involves pH control of the protonation vs hydroxylation reactions occurring at the nanoparticle surface. TEM analysis and Rietveld refinement of XRD data show that three distinct types of heterostructured nanocrystals occur: NiO/$Mn_xNi_{1-x}O$ core–shell-like heterostructures at the pH of 2.4, mixed NiO/$Mn_xNi_{1-x}O$ and/or/Mn_3O_4 core-overgrowth structures for 2.4 < pH < 4.5, and predominantly NiO/Mn_3O_4 core-island structures for pH > 4.5. The magnetic coercivity and exchange bias of the heterostructured nanocrystals vary systematically with the pH of the aqueous solution used to synthesize the samples. The temperature-dependent magnetization and hysteresis loop data are consistent with the nature of overlayer coverage of the NiO core. Our DFT based calculations show that the $Mn_xNi_{1-x}O$ phase has ferrimagnetic properties with a stable spin orientation along the ⟨111⟩ orientation. Furthermore, the calculations show that the magnetic anisotropy constant (K_1) of the Mn_3O_4 phase is considerably larger than that of the $Mn_xNi_{1-x}O$ phase, which is confirmed by our experimental results. The coercivity and exchange bias field are the largest for the NiO/Mn_3O_4 core-island nanocrystals, synthesized at a pH value of 5.0, with robust values of nearly 6 kOe and 3 kOe, respectively. This work demonstrates the tunability of hydrothermal deposition, and concomitant magnetic coercivity and exchange bias properties, of $Mn_xNi_{1-x}O$ and/or Mn_3O_4 nanophase overgrowth over a NiO core with pH, that makes these heterostructured nanocrystals potentially useful for magnetic device, biomedical, and other applications.

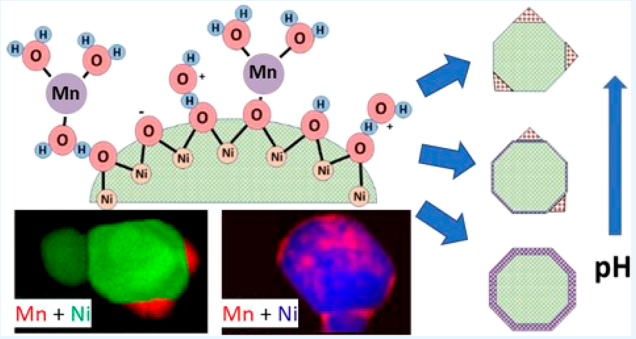

KEYWORDS: *magnetic properties, nanocrystals, hydrothermal synthesis, transmission electron microscopy, exchange bias, coercivity, magnetocrystalline anisotropy, density functional theory*

INTRODUCTION

Bimagnetic multicomponent nanoparticles, either in core–shell, decorated, or more complex assemblies and having a combination of antiferromagnetic and ferro/ferrimagnetic components, have been the subject of intense investigation due to their tunable magnetic properties. Such magnetic heterostructured nanocrystals (MHNCs) have the potential for use in modern-day spintronic devices, magnetic random-access memory (MRAM) devices, drug delivery, ferrofluids, pigments, and hyperthermia.[1−5] The MHNCs are also used in MRI contrast agents in place of conventional gadolinium-based contrast agents, GMR read heads in large capacity hard disk drives whereas their optical properties have been exploited for diagnostic purposes and making organic dyes.[1] Multiple benefits of antiferromagnetic (AFM) based MHNCs are evident, including having nonvolatile memories, increased data processing speeds, size miniaturization, and decreased power consumption, thus making them particularly suitable for spintronic devices.[3,4,6,7] The use of an AFM component, such as CoO, Cr_2O_3, MnO, and NiO, in MHNCs is particularly advantageous because it enables the exchange bias effect spin–spin coupling when assembled with a ferro/ferrimagnetic (FM/FiM) component. The exchange bias effect is vital for enabling the manipulation of the magnetic properties of heterostructured magnetic systems.[8,9] The interface exchange

Received: February 10, 2021
Accepted: May 5, 2021
Published: May 17, 2021

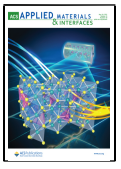

https://doi.org/10.1021/acsami.1c02855
ACS Appl. Mater. Interfaces 2021, 13, 24013–24023

coupling that drives the exchange bias of AFM/FM or AFM/FiM heterostructured nanocrystal systems can be manipulated to control the magnetic coercivity, spin-state switching times, and to overcome the superparamagnetic limit.[10,11] In systems where the AFM magnetic anisotropy energy dominates, the FiM layer spins are pinned toward the direction of the AFM layer raising the magnetic anisotropy of the system through interface exchange coupling.[3,4,12,13] Because the magnetic anisotropy of nanomaterials is highly dependent on the crystalline structure, size, shape, interface quality and composition, having the capability of tailoring such features can be important for achieving robust magnetic anisotropic energies in nanoparticulate heterostructures.[14−18]

Initial work in our laboratory has demonstrated that significant coercivity and exchange bias fields are obtainable for NiO-based and Mn incorporated MHNCs.[2] However, it is not clear from this work how the nature of overgrowth and thereby magnetic properties are controlled by the pH of the aqueous solution used in the hydrothermal synthesis stage of sample preparation. Proton binding on the surface of metallic oxide nanoparticles (NPs) in an aqueous solution (i.e., protonation) is controlled in large measure by the solution pH (see Figure 1).[19] The OH^- ion in aqueous solution is very

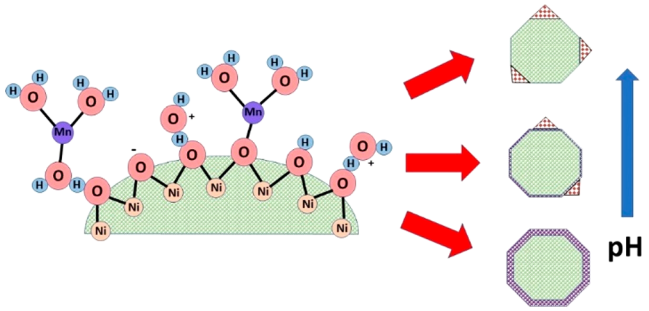

Figure 1. An illustration depicting the adsorption reactions leading to the deposition of Mn^{2+} cations on the surface of a NiO nanoparticle at varying pH conditions; the pH conditions of the solution determine the nature of the heterostructured $Mn_xNi_yO_z$−NiO nanocrystals obtained during synthesis.

reactive in the presence of metal-oxide nanoparticles and reacts with their metal species via the hydroxylation reaction forming >MOH units, where M represents the metal ion and (>) represents the bonds at the surface atomic layer.[20] For NiO nanoparticles, the hydroxylation reaction yields >NiOH units which can be protonated (>NiOH+H^+ → >$NiOH_2^+$) or deprotonated (>NiOH → >NiO^- + H^+), depending on the pH of the aqueous medium. During the initial stages of surface deposition, aqueous metal cations (in this case Mn^{2+}) diffuse through layers of water molecules surrounding the NPs and undergo reactions to form either an inner-sphere complex via a chemical bond (>NiOH + Mn^{2+} → >NiMnO + H^+), an outer-sphere complex via ion pairing (>NiOH + Mn^{2+} → >NiO^-−Mn^{2+} + H^+), or persist within the diffuse swarm of the water molecule layers.[20] As the Mn^{2+} ion has to compete with H^+ ions present in the solution, solution pH becomes a determining factor for the adsorption of Mn^{2+} ions on the NP surface. As the pH of the solution increases, deprotonation of the metal oxide surface increases, resulting in more sites available for the adsorption of Mn^{2+} ions and an increase in the surface deposition. In lieu of our general understanding of these principles, the effect of pH on the size and shape of nanoparticles in hydrothermal synthesis has been successfully interpreted by others.[21,22] Our objective in this work is to understand how the pH affects the Mn-bearing phase overgrowth formation and the magnetic properties of the MHNCs. Here, we discuss the synthesis procedures used to prepare a series of NiO nanoparticles that have to varying degrees a $Mn_xNi_{1-x}O$ and/or Mn_3O_4 overgrowth nanophases, synthesized at pH values ranging from 2.4−7.0. In addition, we discuss the structural, morphological, and magnetic properties of our NiO−$Mn_xNi_{1-x}O$−Mn_3O_4 MHNCs. To our knowledge, this is the first study demonstrating the tunability of the magnetic properties of a bimagnetic multicomponent nanoparticle system using pH of the aqueous solution used in the hydrothermal synthesis stage of the MHNCs.

EXPERIMENTAL AND COMPUTATIONAL DETAILS

The MHNCs were synthesized using a two-step process. The first step follows the procedure described by El Kemary et al.[23] and involves the thermal decomposition of $Ni(OH)_2$ to produce the NiO precursor. First, 0.11 M of aqueous solution under hydrothermal $NiCl_2·6H_2O$ was dissolved in absolute ethanol and then added to NaOH and $N_2H_4·H_2O$. The ratio between $NiCl_2·6H_2O$, $N_2H_4·H_2O$, and NaOH was maintained at 1:5:10. The solution was subsequently stirred well using a magnetic stirrer and dried in an oven under an open atmosphere for 2 h at 600 °C. The thermal decomposition was activated during this step. The resulting NiO powder was rinsed with deionized (DI) water and then centrifuged to remove excess water and residue.

Next, our hydrothermal nanophase epitaxy process was used to grow the Mn-bearing oxide phases over the NiO core.[2,24−26] First, $MnCl_2·3H_2O$ was added to DI water after the water was purged of O_2 using N_2 for 15−20 min at a temperature of 70−80 °C. Eight samples were prepared from aqueous solutions, with pH values ranging from 2.4−7.0 and adjusted by adding drops of HCl or NaOH. Next, 0.33 g of NiO nanoparticles were added to a 0.5 M $MnCl_2·3H_2O$ aqueous solution. After adding NiO nanoparticles to the $MnCl_2$ solution, the mixture was stirred for 25−30 min and then placed in an autoclave. The hydrothermal treatment of each sample was accomplished by placing the autoclave in a furnace for 22.5 h at a temperature of 200 °C. Once the hydrothermal synthesis was complete, the product was rinsed using DI water, centrifuged, and then dried at a temperature of ∼50 °C. Table 1 lists the samples that were prepared using the methodology described above.

XRD measurements of the samples were made using a Bruker D8 Discover diffractometer using a Cu Kα X-ray source with a wavelength of λ = 1.541 84 Å. The diffractometer was operated at 40 kV and 40 mA with a 0.6 mm slit located on the incident X-ray beam side. All XRD patterns were refined using TOPAS software via the Rietveld method. TEM images of the samples were collected using an FEI Tecnai G2 F20 X-Twin microscope at GeoForschungZentrum, Potsdam, Germany, with the field emission gun operating at 200 keV, and equipped with a Gatan Imaging Filter (GIF) Tridiem 863. HR STEM images were collected with a probe-corrected Thermo Fisher

Table 1. List of MHNC Samples, Their Size, and pH Values Used in the Hydrothermal Synthesis Step of Sample Fabrication

sample	B1	B2	B3	B4	B5	B6	B7	B8
pH	2.4	3.0	3.5	4.0	4.5	5.0	6.0	7.0
size (nm)	29.34	29.69	28.74	29.24	25.03	27.74	25.53	24.89

https://doi.org/10.1021/acsami.1c02855
ACS Appl. Mater. Interfaces 2021, 13, 24013−24023

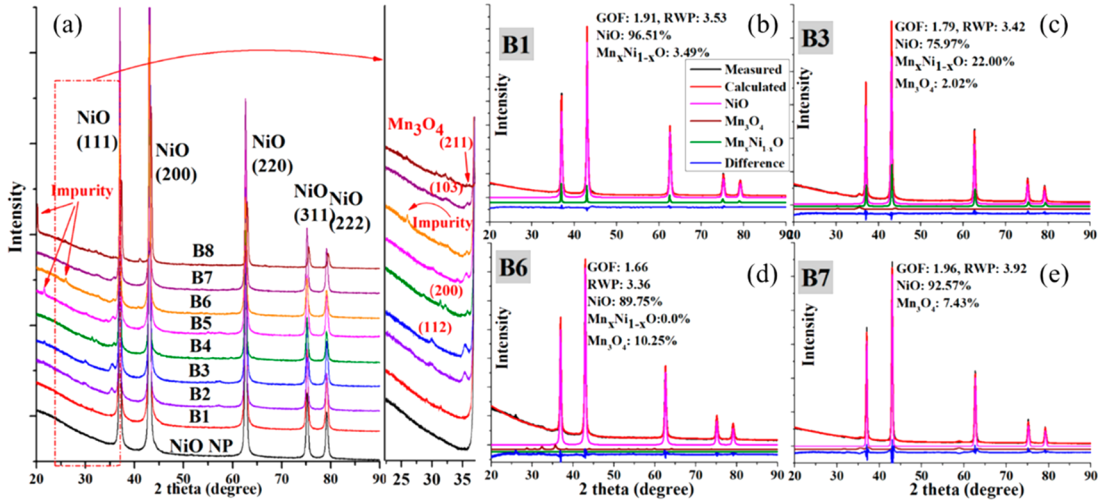

Figure 2. (a) The XRD data collected from the NiO NPs and the MHNC samples; the Rietveld refinement fitting of the XRD data collected from (b) B1, (c) B3, (d) B6, and (e) B7. The fitting of the XRD data measured from the remaining samples is shown in the SI.

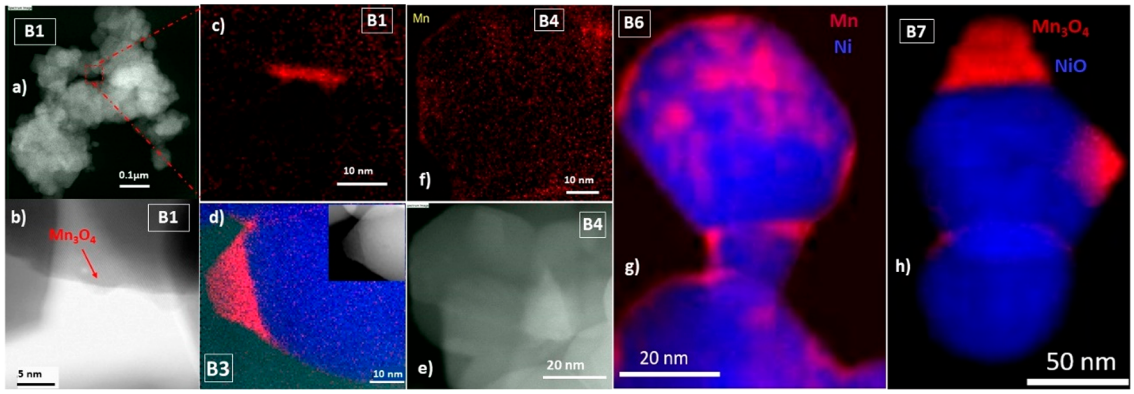

Figure 3. (a) A high-angle annular dark-field (HAADF) image of sample B1 and (b) of a few select B1 nanoparticles outlined in the rectangle in (a); (c) a TEM-EELS Mn elemental map of the same region as in (b); (d) a HAADF image (inset) and a TEM-EELS map showing Mn concentrated in a Mn_3O_4 decorative island and lightly distributed on the surface of the remainder of an isolated B3 nanoparticle; (e) a HAADF image and (f) a TEM EELS Mn elemental map of several B4 nanoparticles. TEM-EELS maps showing Mn and Ni elemental distributions on isolated (g) B6 and (h) B7 nanoparticles.

Scientific Themis Z 3.1 microscope, operating at 300 kV, and equipped with a GIF Continuum 1065. Additional TEM imaging and EELS mapping was made using an FEI Titan 80−300 instrument, located at the University of Arkansas Nano-Bio Materials Characterization Facility, with the field emission gun operating at 300 keV. Magnetic data were measured using a Quantum Design Physical Property Measurement System (PPMS). For the magnetization vs temperature data, for both the field-cooled (FC) and zero-field-cooled (ZFC) measurements, the samples were first cooled to 5 K from room temperature. Furthermore, each sample was cooled in a field of 100 Oe for the FC measurements, whereas the magnetization data were collected in a 100 Oe external field. Both the FC and ZFC hysteresis curves were measured from −18 000 Oe to +18 000 Oe at different intervals and at 5 K. The sample was cooled in a field of 20 kOe for the FC M vs H hysteresis measurements.

Density functional theory calculations were performed using the Vienna Ab initio Simulation Package (VASP) v5.4.1[27] wherein we utilized Projector Augmented-Wave (PAW) pseudopotentials with the Perdew Burke Ernzerhof (PBE) exchange correlational functional.[28,29] The simplified (rotationally invariant) approach to the LSDA+U, introduced by Dudarev et al. were implemented to account for the strongly correlated d-electrons.[30] The effective on-site Coulomb interactions were set to U = 7.60 eV, whereas J = 0 eV was used for the on-site exchange interactions. For all calculations, the energy cutoff was set to 520 eV and an accurate electronic convergence was achieved through setting a free energy change between two self-consistent steps to be less than 1×10^{-5} eV. For electronic structure calculations, a $4 \times 4 \times 4$ K points grid was used based on the Monkhrost-Pack scheme.[31] In order to simulate a dilute Mn concentration (~2.1%) in $Mn_xNi_{1-x}O$, a 96 atoms supercell was used for the electronic structure and energetics calculation. First, a ⟨111⟩ type unit cell containing 8 atoms was constructed through a matrix transformation by using VESTA 3.4.2, whereupon the transformation was facilitated via a correct spin configuration in the NiO supercell ($2 \times 3 \times 2$, 96 atoms) by preserving the symmetry. To calculate the magnetocrystalline anisotropy energy of the $Mn_xNi_{1-x}O$ phase, a $2 \times 2 \times 2$ supercell having 64 atoms was constructed from the rock-salt NiO unit cell, whereas a 24-atom unit cell was utilized for the ferrimagnetic Mn_3O_4 phase. The magnetocrystalline anisotropy energy (E_{MAE}) is defined as follows:

$$E_{MAE} = E_{[uvw]} - E_{min} \quad (1)$$

$E_{[uvw]}$ is the energy of a crystal with spin orientation along the ⟨uvw⟩ direction and E_{min} is the energy having the most stable spin orientation. The anisotropy constant (K_1) was calculated using the following expression:

$$\frac{E}{V} = K_1(\alpha^2\beta^2 + \beta^2\gamma^2 + \gamma^2\alpha^2) \quad (2)$$

https://doi.org/10.1021/acsami.1c02855
ACS Appl. Mater. Interfaces 2021, 13, 24013−24023

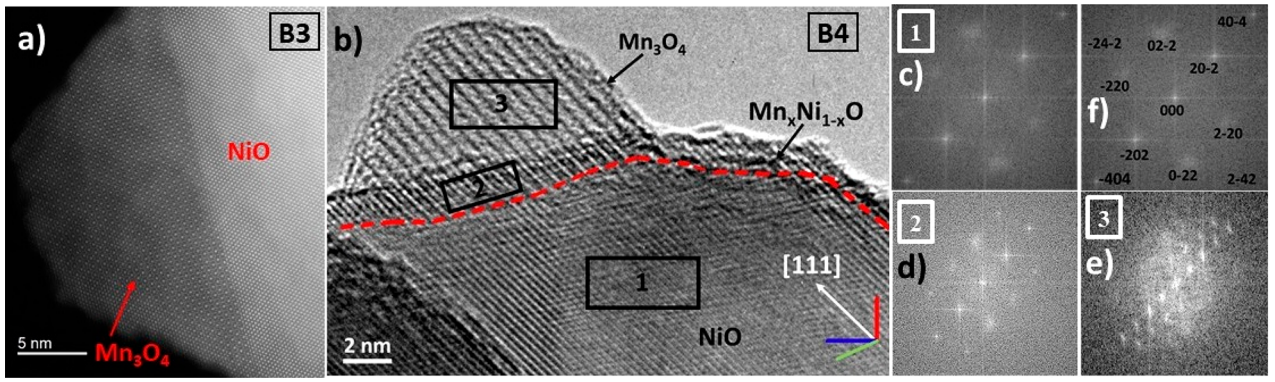

Figure 4. (a) An HRTEM image of the B3 nanocrystal shown in Figure 3(d), showing topotaxial overgrowth of the Mn_3O_4 island over the NiO core. (b) An HRTEM image showing the core, shell, and nanoisland overgrowth on the shell of a B4 nanoparticle; (c) FFT of the NiO core region 1, (d) FFT of the $Mn_xNi_{1-x}O$ shell region 2, and (e) FFT of the Mn_3O_4 island region 3; (f) FFT with the atomic planes identified of the NiO core region 1.

Here, E/V is the anisotropy energy per unit volume, and α, β, and γ are polar coordinate parameters defined according to $\alpha = \cos\Phi * \sin\theta$, $\beta = \sin\Phi * \sin\theta$, and $\gamma = \cos\theta$.

RESULTS AND DISCUSSION

In Table 1 we list the MHNC samples used in this study along with the pH values used during the hydrothermal synthesis step. The Supporting Information (SI) shows low-resolution TEM images depicting the morphology of the nanoparticles. The majority of the nanoparticles have facets whereas the remainder have pseudospherical morphology. Figure 2 shows the XRD data measured from our MHNC samples. The Scherrer equation was used along with peak fitting within TOPAS to estimate the crystallite size of the samples from the XRD data: These values are shown in Table 1. The size of the NiO nanoparticles prior to hydrothermal synthesis was 23.57 nm, as determined using the same method. The XRD patterns clearly show NiO and Mn_3O_4 peaks, along with a limited number of minor impurity phase peaks. The impurity peaks were checked against all known phases involving nickel ± manganese ± oxygen, and do not coincide with these: thus, the nature of these peaks was not confirmed. Detailed Rietveld refinement fitting was made of the XRD data measured from the MHNC samples: Figure 2 and the SI show the structural results from the fitting. The Rietveld refinement fitting of the XRD data is consistent with a $Mn_xNi_{1-x}O$ epitaxial shell formation over the NiO core, with the overgrowth nanophase having the same space group $Fm\bar{3}m$[32] as the NiO precursor nanoparticles. This is supported by the transmission electron microscope−electron energy loss spectroscopy (TEM-EELS) maps shown in Figure 3 that display diffuse and uniform Mn distributions on B1, B3, and B4 nanocrystals consistent with the $Mn_xNi_{1-x}O$ shell-like overgrowth. The XRD peaks attributed to the $Mn_xNi_{1-x}O$ phase of the MHNC samples are shifted relative to those measured from the as-synthesized NiO nanoparticles to lower 2θ values. The observed lattice expansion of this phase is attributed to the larger ionic radius of Mn^{2+} (0.83 Å) compared to that of Ni^{2+} (0.69 Å) in octahedral coordination.[33] The Mn_3O_4 nanophase has a spinel structure with the space group I41/amd.[34] The fitting of the XRD data shows a pH-dependent trend in the presence of hydrothermally grown overgrowth phases in the MHNC samples. Our fitting is consistent with sample B1 having highly predominantly a thin $Mn_xNi_{1-x}O$ (~3.5%) shell overgrowth contribution, which is substantially increased for an intermediate pH sample B3 (~22%). Samples B2 to B4 have a combination of $Mn_xNi_{1-x}O$ and Mn_3O_4 phases whereas samples B5 to B8 have predominantly the Mn_3O_4 overgrowth phase. The largest Mn_3O_4 phase content (10.25%) is observed for sample B6 at pH ≈ 5. Thus, in general, NiO/$Mn_xNi_{1-x}O$ core−shell-like formation occurs at the lowest pH of 2.4 (B1), a mixed NiO/$Mn_xNi_{1-x}O$ and NiO/Mn_3O_4 core-overgrowth occur at 2.4 < pH < 4.5 (B2−B5), and predominantly NiO/Mn_3O_4 core-island structure formation occurs at pH > 4.5 (B6−B8) hydrothermal solution room-temperature values. Our results for Mn_3O_4 overgrowth phase MHNC hydrothermal synthesis at the highest pH value of this study are consistent with the results obtained by Hu et al.[35]

The nature of overgrowth was further investigated using TEM-EELS and high-resolution TEM (HRTEM) imaging of select samples. As indicated by the TEM-EELS maps shown in Figures 3a−f, Mn is predominantly and sparsely distributed in uniform fashion on the surfaces of samples B1, B3, and B4 nanocrystals, which is suggestive of a thin and dilute $Mn_xNi_{1-x}O$ shell overgrowth, with occasional Mn-concentrated Mn_3O_4 nanoisland overgrowths. Figure 3g confirms the presence of Mn in the surface overgrowth regions of B6 nanocrystals. The distribution of Mn in the TEM-EELS map is consistent with predominantly small Mn_3O_4 nanoislands although there are likely minor amounts of partial $Mn_xNi_{1-x}O$ shell regions in the TEM image. Conversely, the TEM-EELS map of isolated B7 nanocrystals in Figure 3h shows only Mn_3O_4 nanoisland overgrowth of the substantial extent and no $Mn_xNi_{1-x}O$ phase. These results are consistent with the analysis of the structural results obtained from the Rietveld refinement fitting of the XRD data measured from the MHNC samples. Additional TEM images and related data are shown in the SI.

Figure 4a shows clear evidence for topotaxial growth of the Mn_3O_4 phase over the NiO core of a B3 nanocrystal. Fast Fourier Transforms (FFTs) of the HRTEM images, such as for example shown in Figure 4b, confirm the presence of Mn_3O_4 nanoislands and/or $Mn_xNi_{1-x}O$ shell regions epitaxially grown on the NiO core of the MHNC samples. As shown in Figure 4b, for samples in which both overgrowth phases are present, the Mn_3O_4 nanoislands may be epitaxially grown over the $Mn_xNi_{1-x}O$ shell regions of the MHNCs. This is evident from the pronounced expansion of the Mn_3O_4 phase lattice parameters for samples B2−B4 as shown in Table S1 of the SI. The spinel structure of the Mn_3O_4 nanoislands reorients to

https://doi.org/10.1021/acsami.1c02855
ACS Appl. Mater. Interfaces 2021, 13, 24013−24023

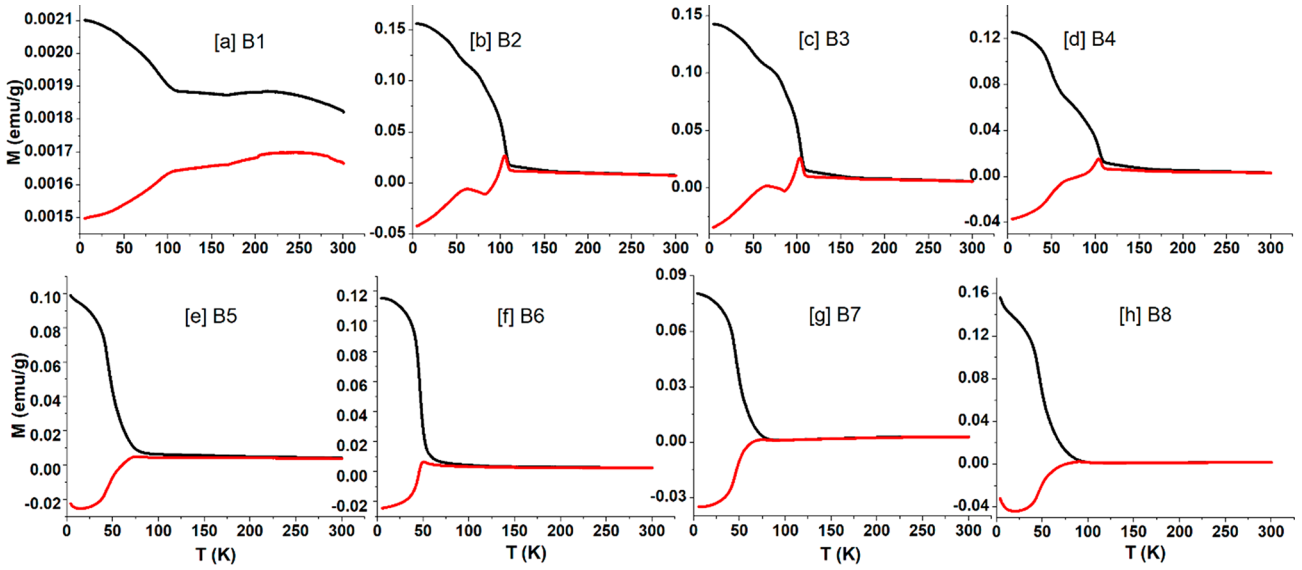

Figure 5. Magnetization vs temperature data measured in the FC (black lines) and ZFC (red lines) conditions for samples: (a) B1, (b) B2, (c) B3, (d) B4, (e) B5, (f) B6, (g) B7, and (h) B8.

Table 2. Blocking and Bifurcation Temperatures of the MHNC Samples

sample		B1	B2	B3	B4	B5	B6	B7	B8
characteristic temp. (K)	T_{C1}		62	63	65	74	50	74	89
	T_{C2}	108	105	103	104				
	T_B	90	103	100	102	45	46	45	46

accommodate the alignment of the cations among the nanophases, with the preferred direction for this reorientation being along the ⟨111⟩ growth direction, as determined from FFT analysis (Figures 4c–f) using Crystbox.[36] This is consistent with a topotaxial overgrowth of the spinel-structured Mn_3O_4 nanoislands over the rock-salt $Mn_xNi_{1-x}O$ or NiO phase.[37] An overall expansion of the Mn_3O_4 lattice parameters evident in Table S1 of the SI for samples B2–B8 may be due to incorporation of OH into the structure at terminal Ni and/or Mn sites into the structure, particularly at interfaces and surfaces. Misalignments due to lattice mismatch and vacancies are visible in Figure 4b at the core/shell/island interface. The defects are due to structural relaxation upon spinel/rock-salt and $Mn_xNi_{1-x}O$/NiO phase overgrowth. In addition, the formation of misfit dislocations and stacking faults occur during the overgrowth of the $Mn_xNi_{1-x}O$ shell and Mn_3O_4 nanoislands. These defects are particularly noticeable near the $Mn_xNi_{1-x}O$-NiO and Mn_3O_4–$Mn_xNi_{1-x}O$ interface regions shown in Figure 4b.

The FC and ZFC magnetization (M) curves measured as a function of temperature (T) from samples B1 to B8 are presented in Figure 5. The ZFC curves increase from an initial negative magnetization value, reach a peak (or show two peaks), and then decrease and generally approach but do not reach a bifurcation point with the FC curves at higher temperatures. The absence of a bifurcation temperature could be due to two reasons: (i) it either exceeds 300 K or, (ii) it may be due to the application of too high of an external field (100 Oe) in the measurement of the M–T curves. There are two peak-like features evident in the ZFC curves for samples B2 and B4 below ∼110 K, which coincide respectively with sudden onsets of increasing FC magnetization with decreasing temperature. For samples B5–B8, the peak occurring in the ZFC curves above 100 K is absent and only the lower temperature peak is present. The rapid increase in the magnetization in the FC curves and the corresponding drop-off in the ZFC curve with decreasing temperature is characteristic of a Curie-like behavior. According to previous studies, the Curie temperature of FiM Mn_3O_4 nanoparticles is ∼42K.[38,39] We identify the low-temperature peak-like feature (T_{C1}), occurring between 62 to 89 K in the ZFC M–T curves, with the freezing of the FiM spins in the Mn_3O_4 islands. As was suggested from our preliminary study and will be more firmly established below, the $Mn_xNi_{1-x}O$ nanophase of the NiO/$Mn_xNi_{1-x}O$ MHNCs has FiM properties.[2] Accordingly, we attribute the higher temperature transition (T_{C2}), occurring in the 103–108 K range in the ZFC M–T curve, with the freezing of the FiM spins in the $Mn_xNi_{1-x}O$ shell layer on the MHNCs. The T_{C1} and T_{C2} values are tabulated for our samples in Table 2. This interpretation is wholly consistent with our results from XRD and TEM analysis, specifically that samples B2–B4 contain both the $Mn_xNi_{1-x}O$ shell and Mn_3O_4 island overgrowth whereas samples B5–B8 have predominantly Mn_3O_4 islands decorating the NiO nanoparticles. The ZFC M–T curve for sample B1 does not exhibit a peak below 100 K: We attribute this to the lack of Mn_3O_4 overgrowth on the MHNCs for the lowest solution pH value (2.4).

Because of interparticle dipolar interactions (due to tightly packed samples for M–T measurements) and nanoparticle finite-size distribution, we use the $-d(FC - ZFC)/dT$ plotted vs temperature to determine the mean blocking temperature ⟨T_B⟩, which we simply refer to as T_B: Note that FC was measured in the warming mode and is thus consistent with this definition.[40] Some of the additional effects which warrant the use of the aforementioned definition for T_B include the presence of uncompensated spins, AFM vs FiM crystalline

https://doi.org/10.1021/acsami.1c02855
ACS Appl. Mater. Interfaces 2021, 13, 24013–24023

anisotropy inherent in our heterostructured nanocrystals, spin clusters, and lattice strain, particularly at the interface between the core and $Mn_xNi_{1-x}O$ shell and/or Mn_3O_4 island overgrowths. We show the plots of $-d(FC - ZFC)/dT$ vs T, used to determine the T_B values, for select samples in the SI. Table 2 shows the T_B values determined for the samples of this study. The larger blocking temperatures (≥90 K) for samples B1−B4 are assigned to the $Mn_xNi_{1-x}O$ overgrowth phase whereas the lower blocking temperatures (~46 K) are assigned to the decorative Mn_3O_4 overgrowth islands. The Néel temperature for AFM NiO nanoparticles having a diameter in the 20−60 nm range has been shown to exceed 350 K.[41] This is consistent with the lack of a blocking temperature being attributed to the magnetically soft AFM NiO core in our MHNCs. We note that the ZFC $M-T$ curves decrease and eventually become negative below T_{C2} for samples B1−B4 or below T_{C1} for samples B5−B8, whereas the FC curves generally increase with decreasing temperature in this range. This effect, which was predicted by Néel and verified for magnetic materials having two or more sublattices with FiM ordering,[42] occurs due to one sublattice of the FiM shell/island nanophase progressively overcoming the contribution due to the other FiM sublattice as the temperature is lowered, in the ZFC case. It is not known how additional effects due to surface and interface anisotropies, lattice strain, and spin clusters may contribute to the FiM sublattice and overall $M-T$ behavior.

Low-temperature (5K) M vs magnetic field (H) hysteresis data ($M-H$ loops), for both the FC and ZFC cases, are presented in Figure 6. The coercivity (H_C), remanent magnetization (M_R), saturation magnetization (M_S), and exchange bias field (H_E) values derived from the hysteresis data for the samples of this study are shown in Table 3. The exchange bias values were calculated using the FC coercivity values from the following formula: $H_E = |H_{C+} - H_{C-}|/2$, where H_{C+} and H_{C-} are the H values where $M = 0$ for the ascending (+) and descending (−) loop portions, respectively. The saturation magnetization was determined by extrapolating values from the M vs $1/H$ graph. Figure 6 indicates that the low-temperature hysteresis loops change significantly with increasing synthesis pH values from sample B1 to B8. The hysteresis loops exhibit the standard letter "S" shape for samples B1−B4 whereas the ones for samples B5−B8 are more linear and tilted-oval type. The hysteresis loops for samples B6 and B7 have particularly large coercivities.

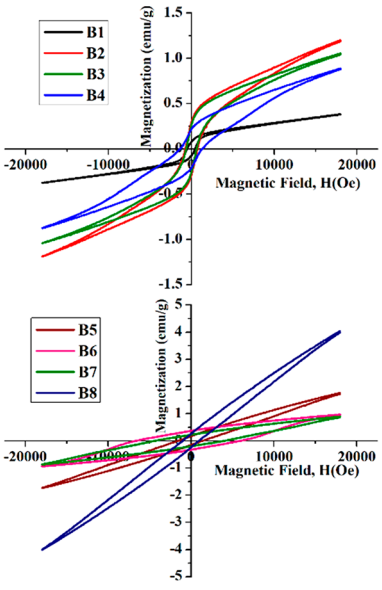

Figure 6. Magnetization (M) vs magnetic field (H) curves for samples B1 to B8 (inset: magnified $M-H$ loops).

As was alluded to above, both the $Mn_xNi_{1-x}O$ and Mn_3O_4 overgrowth phase of our MHNCs have FiM properties. Thus, the trend exhibited by the shape of the hysteresis loops in Figure 6 can be explained by domain-size effects attributed to the overgrowth phases, where the mean domain size appears to be controlled by the pH value used during the MHNC synthesis. In general, the "S" shaped hysteresis loops for samples B1−B4 ($2.4 \leq pH \leq 4.0$) are indicative of multiple domains, whereas the linear-oval shaped hysteresis loops for samples B5−B8 ($4.5 \leq pH \leq 7.0$) are indicative of single domain FiM nanophases.[13,14,43,44] The low coercivity, exchange bias, and remanent magnetization values, along with the hysteresis loop characteristics, for sample B1 (pH 2.4) are consistent with having thin FiM $Mn_xNi_{1-x}O$ shell overgrowth with multiple domains. Sample B6 has the highest H_C and M_R values (see Table 3), indicating that this MHNC specimen has the largest single-domain (SD) structure and FiM phase overgrowth; this is consistent with our TEM imaging of the MHNCs. This is confirmed in a plot of the coercivity and exchange bias vs pH shown in Figure 7. In

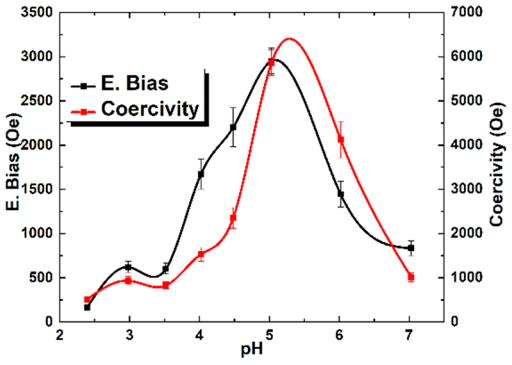

Figure 7. Coercivity and exchange bias of samples B1 to B8. The lines are provided to serve as a guide to the eye only.

Table 3. Saturation Magnetization, Remanent Magnetization (M_R), Coercivity (H_C), Exchange Bias Field (H_E), and Effective Anisotropy Constant (K_{eff}) Derived from the Analysis of the M vs H Hysteresis Data Measured from the MHNC Samples

sample	B1	B2	B3	B4	B5	B6	B7	B8
M_S (emu/g)	0.55	1.32	1.67	0.91	1.88	0.99	0.93	4.37
M_R (emu/g)	0.08	0.29	0.26	0.22	0.18	0.37	0.22	0.26
H_C (Oe)	511.3	934.3	826.0	1530.0	2350.7	5860.4	4122.9	1011.5
H_E (Oe)	165.5	620.8	602.0	1670.9	2199.9	2952.5	1444.6	833.1
K_{eff} (J/m^3)	0.6×10^4				5.1×10^4	4.2×10^4	3.9×10^4	3.9×10^4

https://doi.org/10.1021/acsami.1c02855
ACS Appl. Mater. Interfaces 2021, 13, 24013−24023

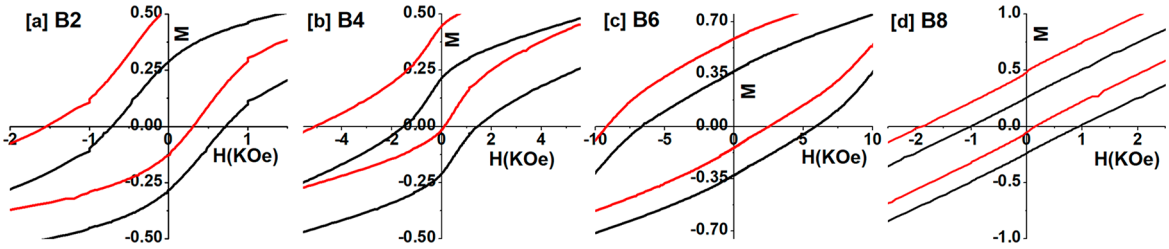

Figure 8. Magnetization vs magnetic field hysteresis curves shown in a range selected to show the shift along the H and M axes of the data measured at 5 K in the field cooled (red line) relative to that of the zero-field cooled (black line) condition of (a) sample B2, (b) sample B4, (c) sample B6, and (d) sample B8.

general, the exchange bias and coercivity exhibit similar dependence with pH value and both peak at a value close to 5. Both the H_E and H_C values are generally and significantly larger for the samples in which the Mn_3O_4 predominates and smaller for samples in which the $Mn_xNi_{1-x}O$ overgrowth phase predominates. This can be attributed to the substantially larger magnetic anisotropy of the FiM Mn_3O_4 than that of the FiM $Mn_xNi_{1-x}O$ overgrowth phase: The anisotropy difference is discussed in greater detail below. We note that the nature of the nanophase, i.e., $Mn_xNi_{1-x}O$ vs Mn_3O_4, has a determinative factor on MD vs SD formation in relation to the physical extent of the overgrowth: The $Mn_xNi_{1-x}O$ phase appears to favor the formation of MD whereas the Mn_3O_4 phase appears to favor SD formation. We attribute this to the effect of starting pH of the aqueous synthesis solution. The adsorption of Mn^{2+} ions is reduced at low pH, due to increasing positive charge from protonation of the NiO nanoparticle surface, and the formation of $Mn_xNi_{1-x}O$ is favored. Conversely, the NiO nanoparticle surface becomes less positively charged as pH is increased leading to more enhanced Mn^{2+}/Mn^{3+} ion adsorption, and the formation of Mn_3O_4 overgrowth on NiO becomes favored over that of the $Mn_xNi_{1-x}O$ phase. This is confirmed by the susceptibility (i.e., dM/dH) vs H data, obtained from the hysteresis loop data measured from the MHNC samples (see Figure S7 in the SI). The reduction in Mn_3O_4 overgrowth at higher pH values (>5) is most likely due to competition between Mn^{2+}/Mn^{3+} ion deposition on the NiO nanoparticle surface and precipitation of manganese hydroxide out of the aqueous solution.

In this section, we examine the nature of the shift between the FC and ZFC hysteresis loops of our MHNCs in more detail. Due to the relatively well-ordered, mostly epitaxial nature of the core−shell/island interface of our MHNCs, there is pronounced spin−spin coupling (i.e., interfacial exchange coupling) and a strong pinning effect at the NiO-overgrowth interface, as evidenced from the magnetization data measured from our MHNCs. The pinning effect plays a pivotal role in increasing the magnetocrystalline anisotropy and exchange bias in the MHNCs.[14−16,38] The FC hysteresis loops shown in Figure 8 are shifted along the negative H axis (H_E) and along the positive M axis relative to the ZFC curves, indicating strong exchange bias fields for our MHNC samples. Furthermore, whereas the H_E values are seen to vary among the samples, and thus with synthesis pH value, the shift of the FC vs ZFC $M-H$ loops along the M axis (i.e., vertical shift) is generally consistent for all samples. The vertical shift of a very similar nature has been attributed to the uncompensated interface spins in FeO/Fe_3O_4 core−shell nanoparticles and other systems.[16,45] In the ZFC case, the uncompensated spins align with the AFM spins at the interface whereas in the FC case, these spins align with the H field but are pinned by the interface AFM spins. The larger positive M values for the ascending portion of the loop occur because this coincides with the alignment of the H field (FC case) and the uncompensated spins, which cannot be flipped (due to being pinned) during the descending portion of the hysteresis loop (H field is reversed), resulting in lower negative M values. Similarly, we attribute the vertical shift of the FC $M-H$ loops measured from our samples to the uncompensated spins at the NiO-overgrowth interface of our MHNCs. The nearly uniform vertical shift of the FC $M-H$ loops is consistent with the uniformity in size and morphology of the NiO precursor nanoparticles used in the synthesis of our B1−B8 samples.

In addition to the interfacial exchange coupling, dipolar interactions (i.e., magnetostatic energy), magnetocrystalline anisotropy, domain structure, morphology, spin canting, and spin clustering are deemed to be important for the manifestation of the magnetic properties of MHNCs. The TEM and magnetization results, including the large H_E values, for our MHNCs are consistent with similar results found for MnO/Mn_3O_4 core−shell nanoparticles.[38] Thus, we infer from these results that the ordered, highly crystalline core-overgrowth interfaces give rise to strong interfacial exchange coupling, which is predominantly responsible for the large H_E values exhibited by our MHNCs. The formation of spin clusters is highly likely on the surface of the faceted Mn_3O_4 islands but much less appreciably on the surface of the $Mn_xNi_{1-x}O$ shell. Nevertheless, due to the relatively larger size of the MHNCs (~25−30 nm), surface spin clusters are not expected to contribute significantly to the exchange bias (EB) effect.

Nanophase Mn_3O_4 has been purported to have a large overall FiM anisotropy, which should have a strong bearing on the magnetic properties of bimagnetic nanoparticles.[38] The AFM anisotropy of NiO nanophases is known to be relatively small in comparison to that of FiM anisotropy of spinel nanophases.[16] The $Mn_xNi_{1-x}O$ shell is a magnetically disordered phase (the Mn spins are not arranged among a periodic magnetic lattice) and thus is expected to have a lower anisotropy. In order to estimate the effective anisotropy constant (K_{eff}) of the Mn-bearing nanophases, we assume weak particle−particle dipolar interactions and use the Kneller formula: $H_C = \frac{2K_{eff}}{M_S}\left(1 - \left(\frac{T}{T_B}\right)^{1/2}\right)$.[46,47] Further assumptions in the use of Kneller's formula include single domain particles having uniaxial anisotropy. As a result, the estimated K_{eff} values should be treated with caution. Table 3 shows our estimates of K_{eff} for samples B1 and B5−B8; the rest of the samples have both the $Mn_xNi_{1-x}O$ and Mn_3O_4 nanophase and their

https://doi.org/10.1021/acsami.1c02855
ACS Appl. Mater. Interfaces 2021, 13, 24013−24023

magnetic data cannot be used to provide unique, single FiM phase anisotropies. The estimated K_{eff} values for the Mn_3O_4 nanophase (samples B5−B8) range from 3.9−5.1 × 10^4 J/m^3 and are considerably larger than for the $Mn_xNi_{1-x}O$ nanophase (sample B1), having a value of 0.6 × 10^4 J/m^3. TheK_{eff} values for the Mn_3O_4 overgrowth phase are on the average roughly half of the anisotropy constant reported for bulk Mn_3O_4.[48] This discrepancy could be due to the deviation from the 1/2 exponential temperature behavior of Kneller's law, dipolar interactions between individual particles, and/or the effect of the dead layer at the surface regions of the Mn_3O_4 overgrowth islands.[47]

COMPUTATIONAL ANALYSIS

Although our preliminary density functional theory (DFT) based calculations suggested that the $Mn_xNi_{1-x}O$ nanophase has FiM ordering below T_C, such results need to be established more firmly.[2] Here, we explore isolated as well as proximal or clustered Mn spins dispersed in a NiO structure, because such populations will potentially modify the nature of the exchange interactions between the cations (Mn−Ni, Mn−Mn, and Ni−Ni). We used DFT based calculations to explore the effects of isolated and proximal Mn spins on the magnetic ordering in $Mn_xNi_{1-x}O$ having dilute Mn concentrations and the rock-salt structure. As shown in Figure 9, our DFT calculations predict

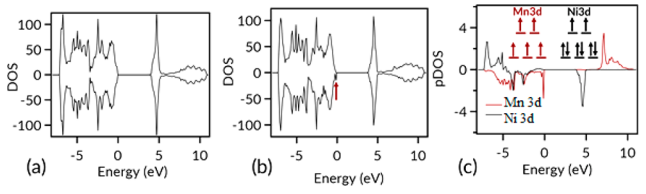

Figure 9. (a) The calculated density of states (DOS) of NiO and of (b) $Mn_{0.021}Ni_{0.979}O$; and (c) partial density of states showing the Ni 3d and Mn 3d contributions to the DOS; the inset shows the spin configuration of the Mn 3d and Ni 3d states.

accurately the AFM properties of NiO: The electronic density of states (DOS) calculation reveals equal spin up and spin down state contributions, resulting in an overall moment of 0 μ_B within the 96 atoms supercell. Single Mn substitution in NiO, which coincides with a 2.1% dilute Mn concentration ($Mn_{0.021}Ni_{0.979}O$), alters the magnetic characteristics from AFM to FiM ordering with a net 2.90 μ_B magnetization for the 96-atom supercell. Examination of the electronic structure of $Mn_{0.021}Ni_{0.979}O$ confirms the FiM characteristics, whereby the incorporation of a Mn atom generates an unequal up and down spin state contribution at the valence band maximum (Figure 9b). The predominant contribution to these new energy states is from the Mn 3d orbitals, as shown from the partial density of state (pDOS) analysis shown in Figure 9c. The electronic band gap of $Mn_{0.021}Ni_{0.979}O$ is 4 eV. The Bader charge analysis reveals that the Mn ion is in +2 oxidation and high spin state, which also holds for Ni ions (inset of Figure 9c). DFT calculations predict a 0.2% expansion in the lattice of $Mn_{0.021}Ni_{0.979}O$, in agreement with the analysis of the XRD data measured from our samples discussed above.

Next, the proximity effects and thereby the clustering tendency of Mn were theoretically explored by substituting two Mn atoms in proximal lattice sites within the 96 atoms supercell of $Mn_{0.042}Ni_{0.958}O$. The proximal two-Mn substitutions are depicted in Figure 10a. The equilibrium spin orientations result in a parallel Mn−Mn spin (↑↑ or FM designation) in-plane substitution ordering case whereas the out of plane substitutions result in antiparallel Mn−Mn spin ordering (↑↓ or AFM designation) cases. To explore which of the substitution cases are energetically favorable, the difference in energy (ΔEnergy) with respect to FM2 (see Figure 10a) was calculated and plotted in Figure 10b. Our DFT calculations suggest that the ↑↓ AFM1 configuration is most energetically favorable in $Mn_{0.042}Ni_{0.958}O$. However, ↑↑ Mn−Mn spin ordered configurations such as FM2 and FM5 are possible with a penalty of only a few meV in energy. Because the magnetic exchange energy does not affect the distribution of Mn ions in the $Mn_{0.042}Ni_{0.958}O$ lattice under hydrothermal conditions utilized for the formation of the overgrowth, all the proximity cases considered in our calculations are equally likely to occur in the $Mn_xNi_{1-x}O$ overgrowth phase. Hence, whether the Mn ions are dispersed or clustered in the epitaxial shell, the substitutional species will induce ferrimagnetic characteristics in $Mn_xNi_{1-x}O$, as evidenced from the sample B1 magnetization vs field data (Figure 5).

The results shown in Figure 7 indicate that the magnetocrystalline anisotropy is an important factor affecting the exchange bias exhibited at low temperatures by our MHNCs. As was discussed above, the nanocrystal overgrowth phases evolve from $Mn_xNi_{1-x}O$ epitaxial shell formation to Mn_3O_4

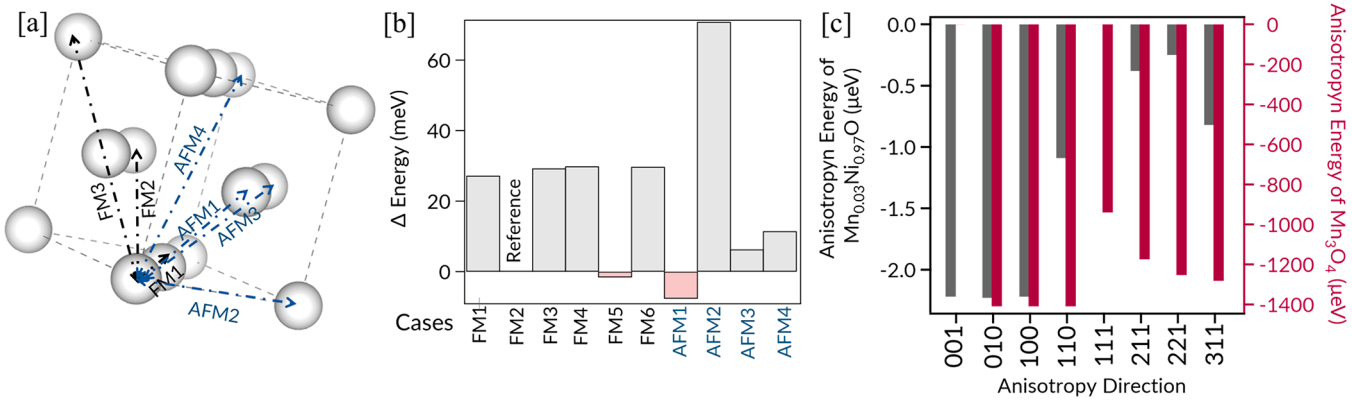

Figure 10. (a) The unit cell showing different configurations of two Mn atom substitution in the $Mn_{0.042}Ni_{0.958}O$ structure; (b) the energy difference (ΔE) plotted for different substitution configurations where the FM2 case is used as a reference; (c) the anisotropy energy of $Mn_xNi_{1-x}O$ and Mn_3O_4 plotted for different anisotropy directions.

https://doi.org/10.1021/acsami.1c02855
ACS Appl. Mater. Interfaces 2021, 13, 24013−24023

island topotaxial growth with increasing (starting) pH value of the hydrothermal solution. This phase evolution as a function of pH was discussed above as the underlying mechanism for the observed trend in the EB effect shown in Figure 7. Using DFT-based theoretical calculations, we have investigated the magnetocrystalline anisotropy energy of $Mn_xNi_{1-x}O$ and Mn_3O_4 (Figure 10c) phases. The calculations predict that the stable spin orientation (i.e., easy axis) for the $Mn_xNi_{1-x}O$ phase is along the ⟨001⟩ direction whereas, for the Mn_3O_4 phase, the easy axis can lie along any of the [100], [010], or [110] directions (Figure 10c). This is consistent with previous magnetic measurements made on preferentially oriented Mn_3O_4 single crystals[48,49] and epitaxially grown thin films.[50] Because the Mn_3O_4 decorative nanoislands result from topotaxial overgrowth on the rock-salt structured NiO or $Mn_xNi_{1-x}O$ phases, we expect that the magnetocrystalline anisotropy for the spinel phase manifest in a similar fashion as for the thin-film system. Furthermore, the calculated magnetocrystalline anisotropy energy for the $Mn_{0.03}Ni_{0.97}O$ phase is considerably lower than the estimated anisotropy energy of the $Mn_xNi_{1-x}O$ overgrowth phase of our MHNCs. Aside from the surface, shape, and other potential anisotropy contributions, this could be attributed to higher Mn content in our MHNCs whereas the calculations were made for dilute concentrations only. Conversely, the calculated magnetocrystalline anisotropy energy for the Mn_3O_4 phase is in overall good agreement with the reported value.[48]

Our experimental and computational results (see Figure 10c) confirm that, because of the considerably larger magnetic anisotropy energy, the Mn_3O_4 overgrowth gives rise to larger EB fields and coercivity values in the MHNCs. The large EB field value for sample B6 (at a pH of 5.0) originates highly predominantly from the Mn_3O_4 phase, which for this pH value results in the deposition of the maximum weight percent of overgrowth of the Mn_3O_4 phase. Conversely, the lowest EB field value was measured from sample B1, which has only the $Mn_xNi_{1-x}O$ epitaxial shell overgrowth in the MHNCs. This is consistent with the magnetometry results from our previous studies, in which we used the hydrothermal nanophase epitaxy technique to synthesize a series of $Cr_2O_3/M_xCr_{2-x}O_3$ (M: Fe, Ni, Co, Mn) epitaxial core−shell nanoparticles.[25,26,51] On the basis of the substitutional cation M, EB fields (20−400 Oe) at 5K were observed for the $Cr_2O_3/M_xCr_{2-x}O_3$ core−shell nanoparticles, which is in the range of the EB field value recorded for sample B1 of the present study.[7,25,26,51] The present study suggests that epitaxial shell formation through 3d transition metal element substitution may induce a small EB effect and a lower coercivity, but heterostructure phase selectivity through regulation of hydrothermal solution pH value presents an opportunity to amplify the magnetic response and may help tailor heterostructured nanoparticles for real-world applications.

CONCLUSIONS

We have used a two-step self-assembly process to synthesize a series of NiO-based and Mn-incorporated inverse magnetic heterostructured nanocrystals (MHNCs) by systematically varying the pH value in the second-step hydrothermal synthesis process from 2.4−7.0. Our TEM and XRD data analyses are consistent with an epitaxial rock-salt $Mn_xNi_{1-x}O$ shell overgrowth and clearly show topotaxial spinel Mn_3O_4 decorative nanoisland overgrowth on a NiO core of the MHNCs. Furthermore, the totality of our results show the $Mn_xNi_{1-x}O$ overgrowth occurs alone in the sample prepared at the lowest pH value (2.4), the Mn_3O_4 nanoislands occur predominantly in samples prepared at pH values of 5.0 and above, and the admixture of the overlayer phases occur in samples prepared at pH values in between. The results from the analysis of the magnetometry data show that the largest values for H_E and H_C occur for heterostructured nanocrystals having predominantly the Mn_3O_4 overgrowth phase, peaking at 3.0 and 5.9 kOe, respectively, for the MHNCs prepared at a pH value of 5.0. Our DFT-based calculations confirm that the $Mn_xNi_{1-x}O$ phase has equilibrium FiM spin ordering below the Curie temperature, with an easy axis along the ⟨001⟩ direction. Furthermore, both our calculations and experimental results show that the magnetocrystalline anisotropy energy of the Mn_3O_4 phase is considerably larger than that of the $Mn_xNi_{1-x}O$ phase. This work demonstrates that by carefully adjusting the pH value of the aqueous solution used in our environmentally benign hydrothermal overgrowth synthesis process, it is possible to tune the nature and amount of Mn-bearing $Mn_xNi_{1-x}O$ and Mn_3O_4 overgrowth phases in NiO-core MHNCs, and thereby tailor their magnetic properties for potential use in spintronic, biomedical, and other applications.

ASSOCIATED CONTENT

Supporting Information

The Supporting Information is available free of charge at https://pubs.acs.org/doi/10.1021/acsami.1c02855.

Additional X-ray diffraction, x-ray photoelectron spectroscopy, and magnetization vs temperature data (PDF)

AUTHOR INFORMATION

Corresponding Author

Robert A. Mayanovic − *Department of Physics, Astronomy and Materials Science, Missouri State University, Springfield, Missouri 65897, United States*; Phone: 417-836-5606; Email: RobertMayanovic@MissouriState.edu

Authors

Abdullah Al Shafe − *Department of Physics, Astronomy and Materials Science, Missouri State University, Springfield, Missouri 65897, United States*; orcid.org/0000-0002-7923-7283

Mohammad Delower Hossain − *Department of Materials Science and Engineering, The Pennsylvania State University, University Park, Pennsylvania 16802, United States*

Vladimir Roddatis − *GFZ German Research Centre for Geosciences, Telegrafenberg 14473, Potsdam, Germany*

Mourad Benamara − *University of Arkansas Nano-Bio Materials Characterization Facility, University of Arkansas, Fayetteville, Arkansas 72701, United States*

Complete contact information is available at: https://pubs.acs.org/10.1021/acsami.1c02855

Author Contributions

All authors have given approval to the final version of the manuscript.

Notes

The authors declare no competing financial interest.

ACKNOWLEDGMENTS

A.A.S. would like to acknowledge partial support from the College of Natural and Applied Sciences at Missouri State

University. The PPMS measurements were performed at the Cornell Center for Materials Research Shared Facilities, which are supported through the NSF MRSEC program (DMR-1719875). This work used the Extreme Science and Engineering Discovery Environment (XSEDE), which is supported by National Science Foundation grant number ACI-1548562. Funding from the European Regional Development Fund and the State of Brandenburg for the Themis Z TEM (part of the "Potsdam Imaging and Spectral Analysis Facility" (PISA)), is gratefully acknowledged. We thank the reviewers for their most helpful comments which have improved the manuscript.

REFERENCES

(1) Scarfiello, R.; Nobile, C.; Cozzoli, P. D. Colloidal Magnetic Heterostructured Nanocrystals with Asymmetric Topologies: Seeded-Growth Synthetic Routes and Formation Mechanisms. *Front. Mater.* **2016**, *3*, 1−29.

(2) Hasan, S.; Mayanovic, R. A.; Benamara, M. Synthesis and Characterization of Novel Inverted NiO @ $Ni_xMn_{1-x}O$ Core-Shell Nanoparticles. *MRS Adv.* **2017**, *2* (56), 3465−3470.

(3) Freire, T. M.; Galvão, W. S.; Freire, R. M.; Fechine, P. B. A. Bimagnetic Core/Shell Nanoparticles: Current Status and Future Possibilities. In *Complex Magnetic Nanostructures: Synthesis, Assembly and Applications*; Sharma, S. K., Ed.; Springer International Publishing: Cham, 2017; pp 83−119.

(4) Estrader, M.; López-Ortega, A.; Estradé, S.; Golosovsky, I. V.; Salazar-Alvarez, G.; Vasilakaki, M.; Trohidou, K. N.; Varela, M.; Stanley, D. C.; Sinko, M.; Pechan, M. J.; Keavney, D. J.; Peiró, F.; Suriñach, S.; Baró, M. D.; Nogués, J. Robust Antiferromagnetic Coupling in Hard-Soft Bi-Magnetic Core/Shell Nanoparticles. *Nat. Commun.* **2013**, *4*, 1−8.

(5) Wang, Y. X.; Zhang, H.; Liu, E. K.; Zhong, X. C.; Tao, K.; Wu, M. L.; Xing, C. F.; Xiao, Y. N.; Liu, J.; Long, Y. Outstanding Comprehensive Performance of $La(Fe, Si)_{13}H_y$/In Composite with Durable Service Life for Magnetic Refrigeration. *Adv. Electron. Mater.* **2018**, *4* (5), 1700636.

(6) Ghosh, M.; Biswas, K.; Sundaresan, A.; Rao, C. N. R. MnO and NiO Nanoparticles: Synthesis and Magnetic Properties. *J. Mater. Chem.* **2006**, *16* (1), 106−111.

(7) Hossain, M. D.; Mayanovic, R. A.; Sakidja, R.; Benamara, M.; Wirth, R. Magnetic Properties of Core-Shell Nanoparticles Possessing a Novel Fe(II)-Chromia Phase: An Experimental and Theoretical Approach. *Nanoscale* **2018**, *10* (4), 2138−2147.

(8) Meiklejohn, W. H.; Bean, C. P. New Magnetic Anisotropy. *Phys. Rev.* **1956**, *102* (5), 1413−1414.

(9) Meiklejohn, W. H.; Bean, C. P. New Magnetic Anisotropy. *Phys. Rev.* **1957**, *105* (3), 904−913.

(10) Thielemann-Kühn, N.; Schick, D.; Pontius, N.; Trabant, C.; Mitzner, R.; Holldack, K.; Zabel, H.; Föhlisch, A.; Schüßler-Langeheine, C. Ultrafast and Energy-Efficient Quenching of Spin Order: Antiferromagnetism Beats Ferromagnetism. *Phys. Rev. Lett.* **2017**, *119* (19), 1−6.

(11) Shick, A. B.; Khmelevskyi, S.; Mryasov, O. N.; Wunderlich, J.; Jungwirth, T. Spin-Orbit Coupling Induced Anisotropy Effects in Bimetallic Antiferromagnets: A Route towards Antiferromagnetic Spintronics. *Phys. Rev. B: Condens. Matter Mater. Phys.* **2010**, *81* (21), 1−4.

(12) Zhang, Y. J.; Wu, L.; Ma, J.; Zhang, Q. H.; Fujimori, A.; Ma, J.; Lin, Y. H.; Nan, C. W.; Sun, N. X. Interfacial Orbital Preferential Occupation Induced Controllable Uniaxial Magnetic Anisotropy Observed in Ni/NiO(110) Heterostructures. *npj Quantum Mater.* **2017**, *2* (1), 1−7.

(13) Johnston-Peck, A. C.; Wang, J.; Tracy, J. B. Synthesis and Structural and Magnetic Characterization of Ni(Core)/NiO(Shell) Nanoparticles. *ACS Nano* **2009**, *3* (5), 1077−1084.

(14) López-Ortega, A.; Estrader, M.; Salazar-Alvarez, G.; Roca, A. G.; Nogués, J. Applications of Exchange Coupled Bi-Magnetic Hard/Soft and Soft/Hard Magnetic Core/Shell Nanoparticles. *Phys. Rep.* **2015**, *553*, 1−32.

(15) Issa, B.; Obaidat, I.; Albiss, B.; Haik, Y. Magnetic Nanoparticles: Surface Effects and Properties Related to Biomedicine Applications. *Int. J. Mol. Sci.* **2013**, *14* (11), 21266−21305.

(16) Nogués, J.; Sort, J.; Langlais, V.; Skumryev, V.; Suriñach, S.; Muñoz, J. S.; Baró, M. D. Exchange Bias in Nanostructures. *Phys. Rep.* **2005**, *422* (3), 65−117.

(17) Lottini, E.; Lopez-Ortega, A.; Bertoni, G.; Turner, S.; Meledina, M.; Van Tendeloo, G.; de Julian Fernandez, C.; Sangregorio, C. Strongly Exchange Coupled Core|Shell Nanoparticles with High Magnetic Anisotropy: A Strategy toward Rare-Earth-Free Permanent Magnets. *Chem. Mater.* **2016**, *28* (12), 4214−4222.

(18) Lavorato, G.; Winkler, E.; Ghirri, A.; Lima, E.; Peddis, D.; Troiani, H. E.; Fiorani, D.; Agostinelli, E.; Rinaldi, D.; Zysler, R. D. Exchange Bias and Surface Effects in Bimagnetic CoO-Core/$Co_{0.5}Ni_{0.5}Fe_2O_4$ -Shell Nanoparticles. *Phys. Rev. B: Condens. Matter Mater. Phys.* **2016**, *94* (5), 1−9.

(19) Demangeat, E.; Pédrot, M.; Dia, A.; Bouhnik-Le-Coz, M.; Grasset, F.; Hanna, K.; Kamagate, M.; Cabello-Hurtado, F. Colloidal and Chemical Stabilities of Iron Oxide Nanoparticles in Aqueous Solutions: The Interplay of Structural, Chemical and Environmental Drivers. *Environ. Sci.: Nano* **2018**, *5* (4), 992−1001.

(20) Stumm, W. *Adv. Chem. Ser.* **1995**, *244*, 1−32.

(21) Ghobadi, N.; Khazaie, F. Fundamental Role of the PH on the Nanoparticle Size and Optical Band Gap in Cobalt Selenide Nanostructure Films. *Opt. Quantum Electron.* **2016**, *48* (2), 1−8.

(22) Singh, R.; Dutta, S. Synthesis and Characterization of Solar Photoactive TiO_2 Nanoparticles with Enhanced Structural and Optical Properties. *Adv. Powder Technol.* **2018**, *29* (2), 211−219.

(23) El-Kemary, M.; Nagy, N.; El-Mehasseb, I. Nickel Oxide Nanoparticles: Synthesis and Spectral Studies of Interactions with Glucose. *Mater. Sci. Semicond. Process.* **2013**, *16* (6), 1747−1752.

(24) Hasan, S.; Mayanovic, R. A.; Benamara, M. Investigation of Novel Inverted NiO@$Ni_xCo_{1-x}O$ Core-Shell Nanoparticles. *AIP Adv.* **2018**, *8* (5), 056305.

(25) Dey, S.; Hossain, M. D.; Mayanovic, R. A.; Wirth, R.; Gordon, R. A. Novel Highly Ordered Core−Shell Nanoparticles. *J. Mater. Sci.* **2017**, *52* (4), 2066−2076.

(26) Hossain, M. D.; Mayanovic, R. A.; Sakidja, R.; Benamara, M. An Experimental and Theoretical Study of the Optical, Electronic, and Magnetic Properties of Novel Inverted α-Cr_2O_3 at α-$Mn_{0.3}5Cr_{1.65}O_{2.94}$ Core Shell Nanoparticles. *J. Mater. Res.* **2017**, *32* (2), 269−278.

(27) Kresse, G.; Hafner, J. Ab Initio Molecular Dynamics for Liquid Metals. *Phys. Rev. B: Condens. Matter Mater. Phys.* **1993**, *47* (1), 558−561.

(28) Kresse, G.; Joubert, D. From Ultrasoft Pseudopotentials to the Projector Augmented-Wave Method. *Phys. Rev. B: Condens. Matter Mater. Phys.* **1999**, *59* (3), 1758−1775.

(29) Blöchl, P. E. Projector Augmented-Wave Method. *Phys. Rev. B: Condens. Matter Mater. Phys.* **1994**, *50* (24), 17953−17979.

(30) Dudarev, S. L.; Botton, G. A.; Savrasov, S. Y.; Humphreys, C. J.; Sutton, A. P. Electron-Energy-Loss Spectra and the Structural Stability of Nickel Oxide: An LSDA+U Study. *Phys. Rev. B: Condens. Matter Mater. Phys.* **1998**, *57* (3), 1505−1509.

(31) Monkhorst, H. J.; Pack, J. D. Special Points for Brillouin-Zone Integrations. *Phys. Rev. B* **1976**, *13* (12), 5188−5192.

(32) Persson, K. Materials Data on NiO (SG:225) by Materials Project https://materialsproject.org/materials/mp-19009/.

(33) Shannon, R. D. Revised Effective Ionic Radii and Systematic Studies of Interatomie Distances in Halides and Chaleogenides. *Acta Crystallogr., Sect. A: Cryst. Phys., Diffr., Theor. Gen. Crystallogr.* **1976**, *A32*, 751−767.

(34) Persson, K. Materials Data on Mn_3O_4 (SG:141) by Materials Project https://materialsproject.org/materials/mp-18759/.

(35) Hu, C.-C.; Wu, Y.-T.; Chang, K.-H. Low-Temperature Hydrothermal Synthesis of Mn_3O_4 and MnOOH Single Crystals: Determinant Influence of Oxidants. *Chem. Mater.* **2008**, *20* (9), 2890−2894.

https://doi.org/10.1021/acsami.1c02855
ACS Appl. Mater. Interfaces 2021, 13, 24013−24023

(36) Klinger, M. *CrysTBox - Crystallographic Toolbox*; Institute of Physics of the Czech Academy of Sciences: Prague, 2015.
(37) Figlarz, M.; Gérand, B.; Delahaye-Vidal, A.; Dumont, B.; Harb, F.; Coucou, A.; Fievet, F. Topotaxy, Nucleation and Growth. *Solid State Ionics* **1990**, *43*, 143−170.
(38) Berkowitz, A. E.; Rodriguez, G. F.; Hong, J. I.; An, K.; Hyeon, T.; Agarwal, N.; Smith, D. J.; Fullerton, E. E. Antiferromagnetic MnO Nanoparticles with Ferrimagnetic Mn_3O_4 Shells: Doubly Inverted Core-Shell System. *Phys. Rev. B: Condens. Matter Mater. Phys.* **2008**, *77* (2), 1−6.
(39) Ichiyanagi, Y.; Yamada, T.; Kanazawa, Y.; Uehashi, T. Magnetic Properties of Mn_3O_4 Nanoparticles. *AIP Conf. Proc.* **2005**, *850*, 1155−1156.
(40) Denardin, J. C.; Brandl, A. L.; Knobel, M.; Panissod, P.; Pakhomov, A. B.; Liu, H.; Zhang, X. X. Thermoremanence and Zero-Field-Cooled/Field-Cooled Magnetization Study of (Formula Presented) Granular Films. *Phys. Rev. B: Condens. Matter Mater. Phys.* **2002**, *65* (6), 1−8.
(41) Tadic, M.; Nikolic, D.; Panjan, M.; Blake, G. R. Magnetic Properties of NiO (Nickel Oxide) Nanoparticles: Blocking Temperature and Neel Temperature. *J. Alloys Compd.* **2015**, *647*, 1061−1068.
(42) Kahn, O. The Magnetic Turnabout. *Nature* **1999**, *399* (6731), 21−23.
(43) Shloimys, M. I. Hitchhiker's Guide to Magnetism. *Environ. Magn. Work.* **1974**, *279* (1), 1−48.
(44) Morrish, A. H. *The Physical Principles of Magnetism*; IEEE: New York, 2001.
(45) Sun, X.; Frey Huls, N.; Sigdel, A.; Sun, S. Tuning Exchange Bias in Core/Shell FeO/Fe_3O_4 Nanoparticles. *Nano Lett.* **2012**, *12* (1), 246−251.
(46) Kneller, E. F.; Luborsky, F. E. Particle Size Dependence of Coercivity and Remanence of Single-Domain Particles. *J. Appl. Phys.* **1963**, *34* (3), 656−658.
(47) Batlle, X.; García Del Muro, M.; Tejada, J.; Pfeiffer, H.; Görnert, P.; Sinn, E. Magnetic Study of M-Type Doped Barium Ferrite Nanocrystalline Powders. *J. Appl. Phys.* **1993**, *74* (5), 3333−3340.
(48) Dwight, K.; Menyuk, N. Magnetic Properties of Magnetic Properties of Mn_30_4 and the Canted Spin Problem. *Phys. Rev.* **1960**, *119* (5), 1470−1479.
(49) Suzuki, T.; Katsufuji, T. Magnetodielectric and Magnetoelastic Properties of Spinel Mn_3O_4. *J. Phys.: Conf. Ser.* **2009**, *150* (4), 042195.
(50) Ren, L.; Wu, S.; Yang, M.; Zhou, W.; Li, S. Magnetic Properties of Mn_3O_4 Film under Compressive Stress Grown on $MgAl_2O_4$ (001) by Molecular Beam Epitaxy. *J. Appl. Phys.* **2013**, *114* (5), 053907.
(51) Hossain, M. D.; Mayanovic, R. A.; Dey, S.; Sakidja, R.; Benamara, M. Room-Temperature Ferromagnetism in Ni(II)-Chromia Based Core−Shell Nanoparticles: Experiment and First Principles Calculations. *Phys. Chem. Chem. Phys.* **2018**, *20* (15), 10396−10406.

https://doi.org/10.1021/acsami.1c02855
ACS Appl. Mater. Interfaces 2021, 13, 24013−24023